



Efficient removal of methylene blue dye by iron nanoparticles synthesized by a novel green method using jujube leaf extract: characterization, kinetics, and isotherm studies

G. Venkatesan¹ · S. Koteswaran¹ · M. Rengasamy² · R. Rajeshkannan³ · V. Saravanan³ · S. Sujatha⁴ · Panchamoorthy Saravanan² · M. Rajasimman³

Received: 18 May 2023 / Revised: 27 October 2023 / Accepted: 28 October 2023
© The Author(s), under exclusive licence to Springer-Verlag GmbH Germany, part of Springer Nature 2023

Abstract

The most promising eco-friendly green synthesized iron nanoparticles (FeNPs) using jujube leaf extract to decolorize methylene blue (MB) dye was established. Synthesized nanoparticles were characterized through different techniques like TEM, SEM, and FTIR. Various parameters such as dye concentration (5 to 20 mg L⁻¹), nanoparticles load (0.5 to 2.5 mg), temperature, pH, and contact time (30 to 150 min) were optimized. A maximum MB dye removal efficiency of 93.5% is achieved at a time interval of 150 min, temperature 30 °C and pH 9 with 2.5 mg FeNPs for a concentration of 20-mgL⁻¹ methylene blue. The adsorption behavior was monitored using a wide range of isotherm models which includes Freundlich, Dubinin–Radushkevich, Langmuir, and Temkin. The Elovich and intraparticle diffusion models, as well as the dynamical models of pseudo-first- and pseudo-second order has been analyzed for the data obtained from dynamic adsorption. Experimental results were consistent along the paradigm of pseudo-second order. Langmuir adsorption isotherm well suited for adsorption data across exclusive concentration range in comparison to other models. The green synthesized FeNPs has high sorption capacity (1000 mg/g) and environmentally friendly in nature, makes it a potential candidate for wastewater treatment applications.

Keywords Iron nanoparticles · Methylene blue · Dye removal · Green synthesis · Jujube leaf extract · Kinetics · Isotherm

1 Introduction

Dyes find its utilization in various industries such as textile, paper, printing, and in other sector which produce a large amount of harmful colored effluent that endangering environmental protection. In textile industries, dyes are majorly utilized due to their brilliant colors and excellent durability.

Because of their complicated structure, high chroma, and toxicity, traditional procedures like biological treatment, adsorption [1], filtration [2], and coagulation [3, 4] are facing challenges for the removal of azo dyes [5, 6]. Hence, a new approach to deal the dye effluent is required. Iron nanoparticles (FeNPs) are nanoparticles with high activity and inexpensive, shown extraordinary possibility in treating dye effluent as well as color in recent years [7]. As a result, developing a simple, environmentally friendly approach for manufacturing high-performance FeNPs capable of removing dye molecules is vital. By virtue of their distinctive features and their applications in the field of science, technology, and medicine, the production, modification, and usage of nanoscale-level materials as well as nanoparticles has tempted interest [8].

Researchers have created iron nanoparticles from plant extracts and utilized them to adsorb color from aqueous solution. Because of the polyphenol concentration in plants, which is hypothesized to convert iron ions to zero-valent iron, plant extracts are employed as reducers.

✉ M. Rengasamy
mrengasamy40@gmail.com

¹ Department of Civil Engineering, University College of Engineering-BIT Campus, Anna University, Tiruchirappalli 620 024, India

² Department of Petrochemical Technology, University College of Engineering-BIT Campus, Anna University, Tiruchirappalli 620 024, India

³ Department of Chemical Engineering, Annamalai University, Annamalai Nagar, Chidambaram, India

⁴ Department of Chemical Engineering, St. Joseph's College of Engineering, Chennai, India

Therefore, it is crucial for researchers to develop efficient and effective oxide nanomaterial employing environmentally friendly techniques. One of the more environmentally friendly methods is to use plant extracts to reduce metallic salts and produce nanoparticles. It is a simple, affordable, environmentally responsible, and safe for applications. Recently, green generated iron oxide nanoparticles containing plant extracts have been used for the adsorptive removal of colors [9].

Being eco-friendliness, cost-effectiveness, repeatability, and large-scale manufacturing, green and metal nanoparticles biosynthesis has grabbed a lot of spotlight among synthesis methods [10–12]. FeNPs are nanoscale metal fragments that are employed in the conversion of solar energy, biological applications, drug administration, and also in an engine [13]. Many pathogenic bacteria and fungi are toxic to FeNPs [14]. FeNPs manufactured from biobased materials has drawn a lot of interest in nanoscience and technology because of their unique features and applications. The photocatalytic removal of organic dyes by plant extract nanoparticles is time-dependent, with no activity drop until the nanoparticles are reused [15]. FeNPs were created using microbes, enzymes as well as from plants [16, 17]. Plant-derived materials are chosen over animal-derived materials, because they include more bioactive compounds and secondary metabolites which are lessened and also act as an agent for closing for the formation of FeNP [18]. Number of reports on plant-based FeNP generation has been available [19–21].

Plant extracts have been proposed as a basic and safe method of producing nanoscale metals. Various biomolecule-rich plants have been suggested as possible candidates for producing organic Fe NPs [22]. *Ziziphus jujuba* is a Rhamnaceous deciduous plant found in tropical and subtropical countries and the neighboring regions. The *Z. jujuba* mill tree is referred to as jujube in India. Stale jujube, typically, fruits are utilized as food and flavoring, and food additive due to its abundant nutritional value worth. According to recent studies, the *Z. jujuba* plant's extract contains a variety of long-chain chemical substances, the following: fatty acids, alpha-tocopherol, beta-carotene, phenolic compounds, flavonoids, sterols, tannins, alkaloids, and saponin serve as a capping agent and stop the NPs. Flavonoids from jujube fruit have suitable reducing properties, making them excellent reducing agents for the synthesis of environmentally friendly nanoparticles [23, 24]. The novelty of this work is the green synthesise of iron nanoparticles (FeNPs) using jujube leaf extract and employ it to decolorize methylene blue (MB) dye. A complete characterization of the fabricated iron nanoparticles (FeNPs) was also performed. The present study is an attempt to synthesis and characterize the FeNPs using jujube leaf extract and to estimate the removal efficiency of methylene blue dye.

2 Materials and methods

2.1 Plants and chemicals

The reducing substance in the production of iron nanoparticles was jujube leaf juice. The jujube plant leaves were freshly gathered from Anna University's Engineering College, BIT Campus, Tamil Nadu, India. Ferric chloride is purchased from the Himedia Private Limited, India. It is used as a precursor in the experiments.

2.2 Chemicals

Analytical grade ferric chloride and methylene blue (MB) dye were purchased from Merck, India. All chemicals are used without further purification.

2.3 Preparation of jujube leaf extract

Jujube leaf extract was generated in the following manner. Jujube leaves were harvested and washed with normal water for four to five times. Finally, the leaves were washed with distilled water. After that, the tree leaves were cleaned and chopped into little pieces in order to generate the extract in a simpler way. Six grams air-dried jujube leaves soaked in 50 ml of double-distilled water. To separate the jujube stems, this mixture was heated to 100 °C in an Erlenmeyer flask for 30 min. Whatman No. 1 filter paper was used to separate the filtrate. For further testing, the extract was collected and kept in a clean, dry, and air tight container.

2.4 Fabrication of iron nanoparticles using jujube leaf extract

Fifty milliliters of 10^{-3} M ferric chloride is added to the extract solution. Within 2 h, light orange color change is observed, which indicates the presence of iron nanoparticles. The solution is allowed to age for 48 h to yield a deep orange/brown color. The visual observation of the color change during the reaction is given in Fig. 1. The extract is filtered using Whatman filter paper (No. 42) to separate the large aggregates. The extract is then lyophilized to get the iron nanoparticles.

2.5 Dye removal

The catalytic activity of green synthesized iron nanoparticles was tested for methylene blue dye removal. A stock solution of dye was prepared, and various concentrations were prepared using double-distilled water (5 mg, 10 mg, 15 mg, 20 mg, and 25 mg). 0.5 mg, 1.0 mg, 1.5 mg, 2.0 mg,



Fig. 1 Visual observations for the formation of iron nanoparticles (a reaction mixture (a) before reaction, b) after reaction)

and 2.5 mg of green generated FeNPs were added to 100 ml of dye solution separately in each flask. The content was stirred in a magnetic stirrer for a specified length of time. The time was varied from 30 to 150 min, and samples (3 ml) were taken at a time interval of 30 min. UV–visible spectrophotometer was used to track the reaction progress by ensuring dye absorbance maxima at several time intervals, such as 30 min, 60 min, 90 min, and 150 min. An absorbance control set lacking FeNPs was preserved for each color and measured. A calibration curve for methylene blue was built using % absorbance and standard dye solutions belonging to different strengths. Using value of absorbance as a starting concentration, treated dye sample concentration was estimated. Removal efficiency belonging to methylene blue determined is as follows:

$$Y(\%) = \frac{(C_o - C_i)}{C_o} \times 100 \quad (1)$$

The initial and final MB dye concentrations are C_o and C_i respectively. All tests were performed three times. The most significant variance was estimated as 3%. Adjustments were made to pH, temperature, adsorbent dose, interaction duration, and initial MB dye concentration. The equilibrium adsorption quantity, q_e (mg/g), was computed as follows:

$$q_e = \frac{V(C_o - C_e)}{M} \quad (2)$$

In the liquid phase, the initial and steady dye amounts are C_o and C_e (mg/l).

The amount of the solution is V (L), and M stands for the desiccated sorbent's bulk (g).

2.6 Characterization of iron nanoparticles

Gas chromatography-mass spectrometry, (Perkin Elmer Spectrum RX1), Fourier transform infrared spectrometer, (USA (GC–MS, Shimadzu Model No. GC–MS QP 2010 plus, Japan)), and X–ray diffractometer (X-ray

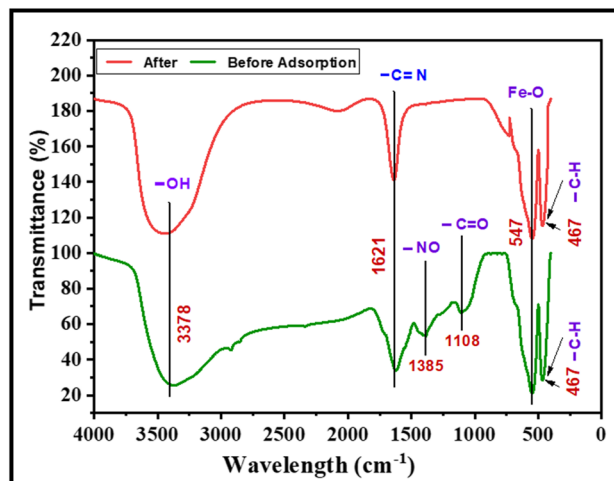


Fig. 2 FTIR spectra of the green synthesized iron nanoparticles (FeNPs) before and after adsorption

diffractometer, X'Pert Pro PANalytical diffractometer, Netherlands) were utilized for evaluating the formation and stabilization of iron oxide nanoparticles. The structure and chemical composition of iron nanoparticles were determined using scanning electron microscopy and energy dispersive X-ray spectroscopy (SEM, TESCAN, Czech Republic) (EDX, OXFORD instruments, UK), and then projected using VEGA3 software. The size distribution was determined using transmission electron microscopy (TEM, Technai T20; Philips).

3 Results and discussion

3.1 Characterization of synthesized FeNps

FTIR spectra of jujube leaf extract were used to identify the biomolecules responsible for synthesizing green synthesized iron nanoparticles (GSFeNPs). Figure 2 shows the FTIR spectrum of green generated iron nanoparticles before and after adsorption. The FTIR spectrum belonging to green-produced iron nanoparticles displays rise at 3378, 2923, 1621, 1385, 1108, 547, and 467 cm^{-1} . Band at 3378 cm^{-1} was allocated to polyphenol hydroxyl group. Unique peaks at 2923 and 1621 cm^{-1} were assigned for amide's nitrile ($-\text{C}-\text{N}$) and carbonyl ($-\text{C}-\text{O}$) groups, respectively. Peaks at 1385 might be due to the $-\text{N}-\text{O}$ bending. The stretching of the $-\text{C}-\text{N}$ sensation in aliphatic amines was related to the absorption band at 1108 cm^{-1} . Iron crystal deformation at the $\text{Fe}-\text{O}$ nanoscale was associated with a strong absorption peak at 547 cm^{-1} . CH_2 group $-\text{C}-\text{H}$ bending vibration was observed to have a typical peak at 467 cm^{-1} . A similar discovery has been made in the past. Twenty absorption lines at 3378, 2923, 1621, 1385, 1108, 547, and 467 cm^{-1} indicate

the presence of polyphenols and proteins around the generated iron nanoparticles. Biomolecules included in jujube leaf extract such as polyphenols and proteins are accountable for the durability of iron nanoparticles and the decrease of Fe^{3+} ions [25, 26]. After adsorption of MB iron nanoparticles, the two bands shifted to 1385 and 1108 cm^{-1} , respectively. The shifts could have been caused by the interaction between MB molecules and iron nanoparticles. In comparison with iron nanoparticles, the adsorption band at 547 cm^{-1} of iron nanoparticles bond shifted slightly. Moreover, considering the rapid adsorption rate, the adsorption process might be mainly controlled by chemical adsorption.

3.2 X-ray diffraction analysis

XRD spectrum with CuK radiation = 1.504 \AA across a broad range of Bragg angles 20° – 90° was used to estimate the particles average size and crystalline nature. Figure 3 and Table 1 illustrate the XRD spectrum of the FeNPS synthesized with various diffraction peaks. The information obtained matched the JCPDS (Joint Committee on Powder Diffraction Standards) File No. (39–1346). By measuring the width of the Bragg's reflection, the approximated dimension of the synthesized iron nanoparticles was estimated as 47 nm . For an average size, by utilizing Scherrer equation ($d = k/\cos$), where the X-wavelength ray (1.54 \AA), the Scherrer constant (0.54). There were no differentiating sharp diffraction peaks because the large diffraction patterns of the peaks were overlapping. This might be due to the ephemeral character of iron nanoparticles.

Fig. 3 XRD pattern of phyto-synthesized FeNPs prepared using jujube leaf extract

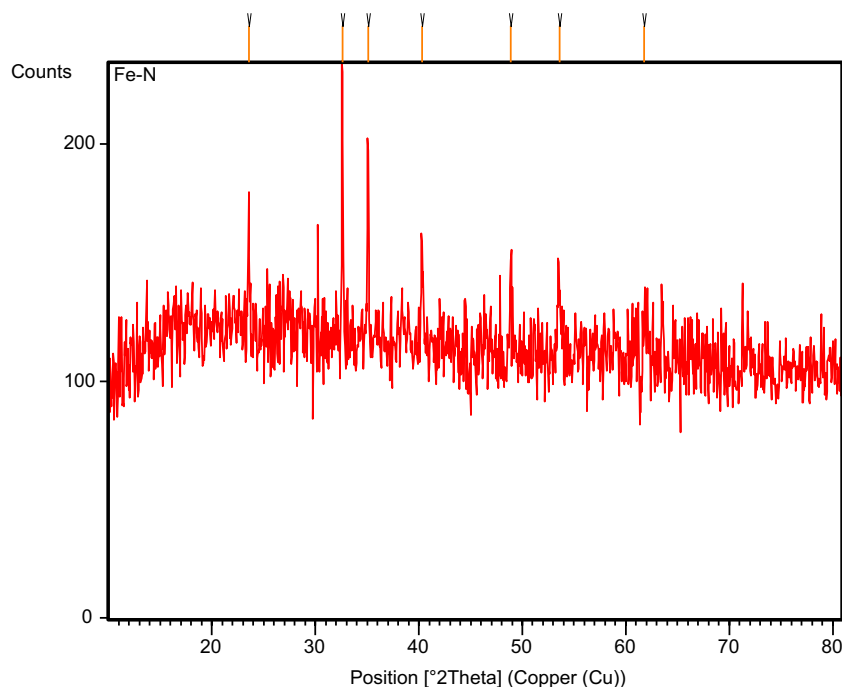


Table 1 Data obtained from XRD

Pos. [$^\circ 2\text{Th.}$]	Height [cts]	FWHM Left [$^\circ 2\text{Th.}$]	d-spacing [\AA]	Rel. Int. [%]
23.5891	40.69	0.2952	3.77165	35.11
32.6159	115.88	0.1476	2.74550	100.00
35.1012	89.24	0.1476	2.55660	77.01
40.3315	40.85	0.2952	2.23630	35.25
48.9153	30.60	0.2952	1.86207	26.40
53.5758	28.20	0.5904	1.71057	24.33
61.7501	15.17	0.4920	1.50231	13.09

3.3 Scanning electron microscopic analysis

Figure 4 shows two different magnifications of SEM images of produced iron nanoparticles using jujube leaf extract. The created nanocrystals of iron were generally spherical and size ranges from 20 to 40 nm (Fig. 5). The size and pattern of iron nanoparticles were changed. This could be as a result of nanoparticles accumulation. According to literatures, the presence of biomolecules on iron nanoparticles surface may be the cause for their aggregation [27, 28].

3.4 EDX analysis of iron nanoparticles

To determine the elemental make up belonging to the synthesized iron nanoparticles, EDX analysis was utilized. EDX iron nanoparticles range was depicted in Fig. 5. According to spectra, they were primarily made up of iron, sodium, and

Fig. 4 SEM images of the iron nanoparticles: **a** at 100 nm and **b** at 40 nm

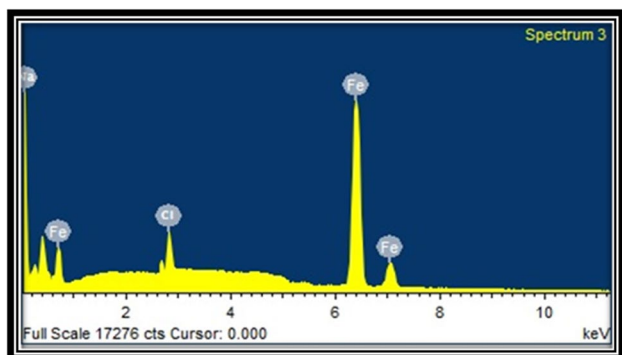
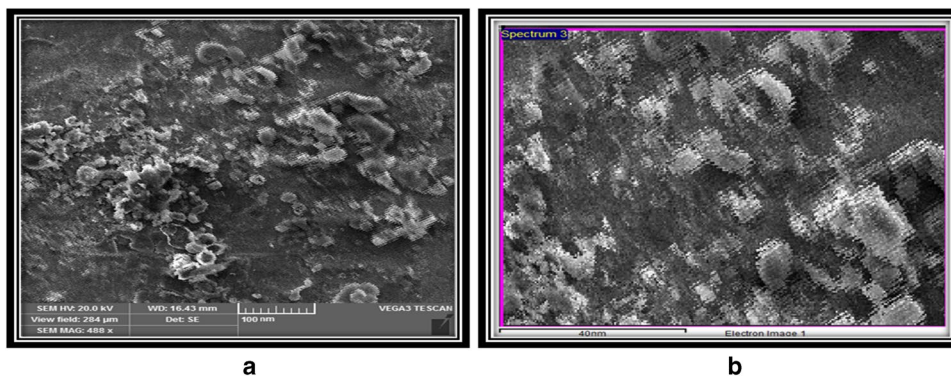


Fig. 5 EDX spectrum of the formed iron nanoparticles

Table 2 Mass percentage of iron nanoparticles as per EDX

Element	Atomic%	Weight%
Fe K	53.02	36.10
NaK	42.94	40.40
Cl K	4.04	23.50
Total		100

chlorine atoms. The presence of carbon and sodium might be due to biomolecules in jujube leaf extract that serve as capping agents. They found comparable results when eucalyptus foliage compounds were used by Wang et al. [29] to create iron nanoparticles. Mass percentages of the generated iron nanoparticles are shown in Table 2. According to the table, the mass proportion of iron component in the produced nanoparticles was 36.1%. It was determined that the produced nanoparticles were in the form of iron using the EDX spectrum and EDX table.

3.5 Transmission electron microscopes

The size, shape, and structural image of synthesized FeNPs are validated using TEM. The presence of iron were found to be round in TEM images (Fig. 6a, b, c, and

d). Size distribution of produced FeNPs is in the range of 10 to 30 nm. The FeNPs generated has an average size of 20 nm.

3.6 Effect of solution pH on biosorption

The impact of pH on MB adsorption was investigated at various pH values of 3, 5, 7, 9, and 11, and the result is demonstrated in Fig. 7. It is evident that under alkaline circumstances, the adsorption of MB rises and at a pH of 9, the maximum adsorption capacity was observed. A reduced adsorption capacity was observed at pH values under 7. The surface will be positively charged and repel positively charged MB particles at pH levels lower than 3. Adsorption of MB increased with a higher pH and decreased with a lower pH, according to the majority of studies [30, 31]. Because it is cationic, MB is drawn to negative charges. The surface of the biosorbent will be positively charged in an acidic environment. The large concentration of H⁺ ions reduces the negative charges from the carboxyl and hydroxyl groups [32]. The surface will be more negatively charged at a higher pH, which will strengthen the electrostatic attraction between the pollutant and sorbent. The negative charge will increase as the carboxyl and hydroxyl groups fully deprotonate [32].

3.7 Effect of solution temperature on biosorption

In the range of 30, 40, 50, and 60 °C, the impact of temperature on sorption was examined. The results are displayed in Fig. 8. Since it is obvious that adsorption works best at lower temperatures, the intermolecular interactions between the MB molecules and the sorbent may become weaker as a result of the elevated temperature, according to literature [33]. Knowing how temperature affects adsorption is crucial since heating the mixture would consume a lot of energy and cost money. The process can be carried out effectively and safely at room temperature.

Fig. 6 TEM images of FeNPs at different magnifications: **a** 5 nm, **b** 5 nm, **c** 10 nm, and **d** 20 nm

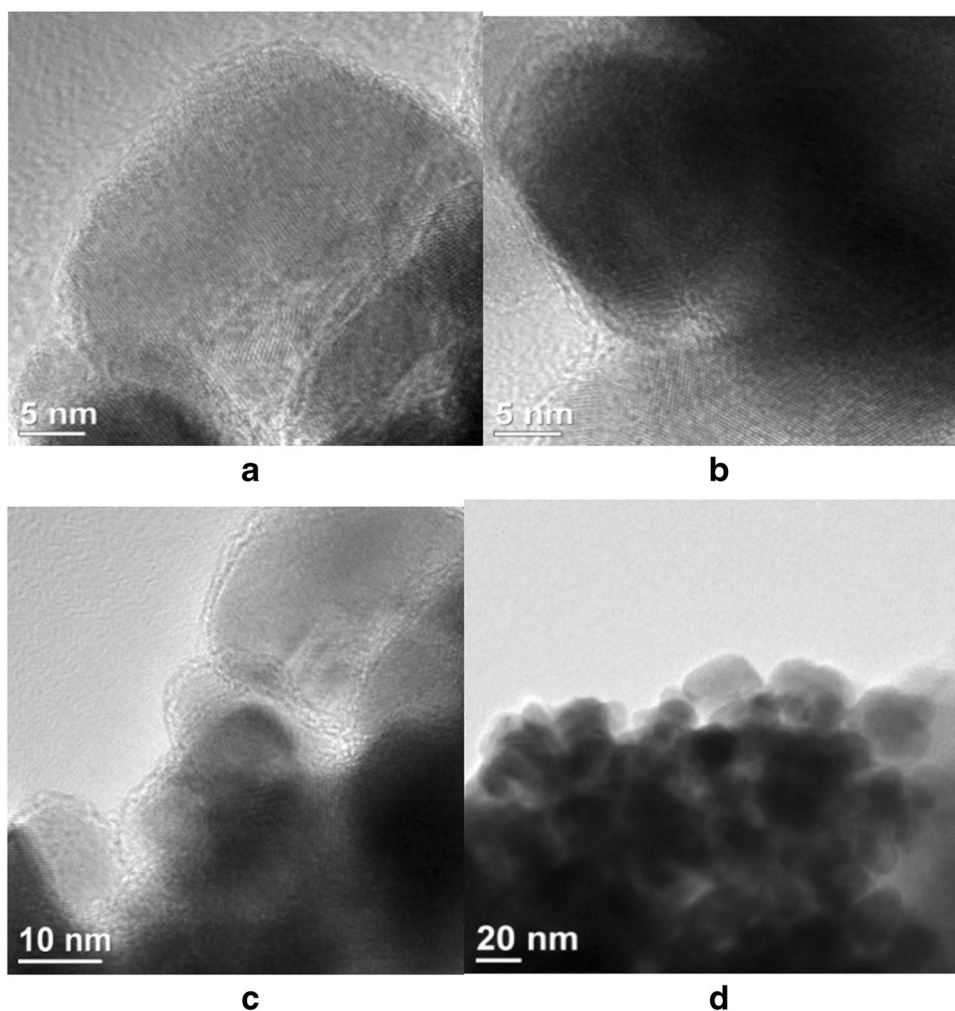
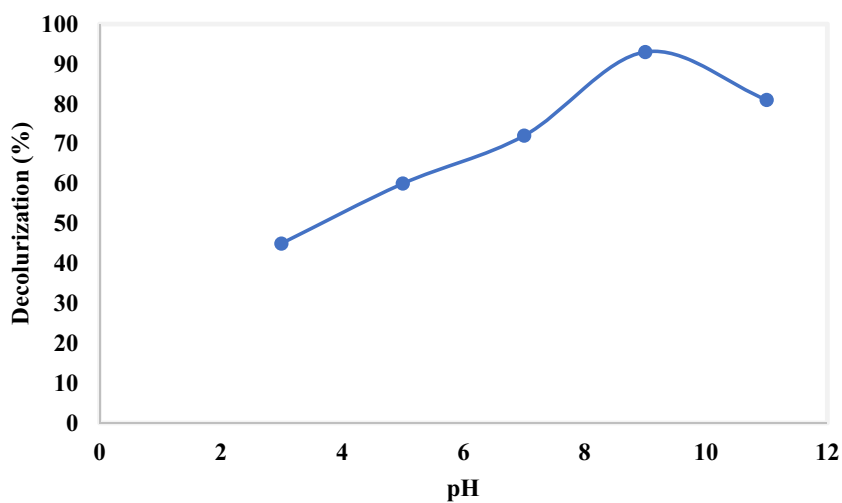


Fig. 7 Solution pH impact on the MB dye removal (time interval — 150 min; temperature — 30 °C; FeNPs — 2.5 mg)



3.8 Effect of contact time on biosorption

Impact of contact time (30–210 min) on MB sorption was investigated and the outcomes are shown in Fig. 9. It was

discovered that, as contact time increases, the MB adsorption rises. The equilibrium was attained after 150 min, i.e., the adsorption sites were completely saturated. When most of the sites are occupied, saturation occurs because the

Fig. 8 Solution temperature impact on the MB dye removal [time interval — 150 min; pH — 9; FeNPs — 2.5 mg]

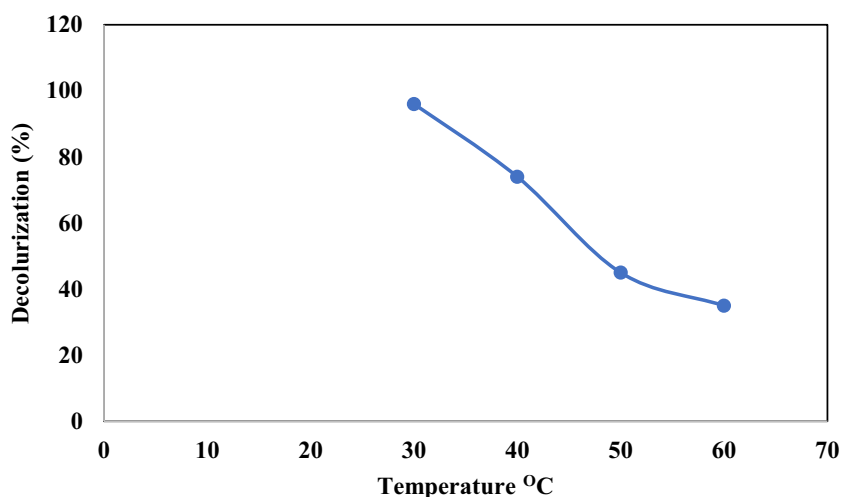
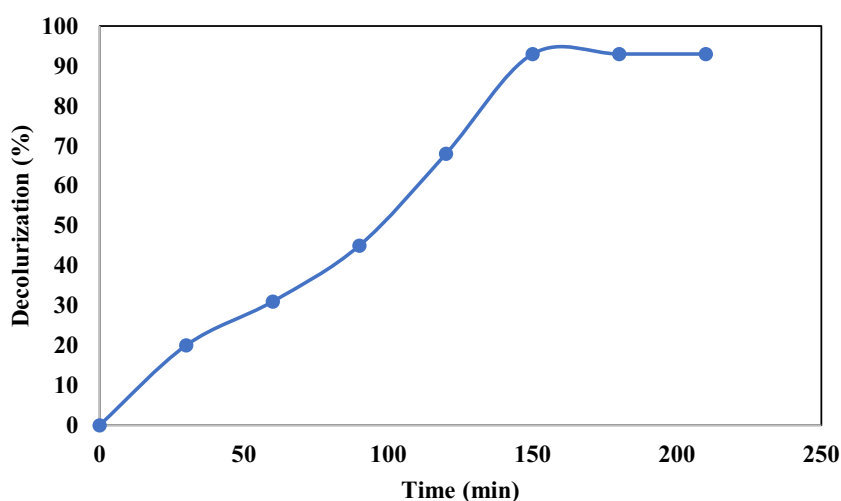


Fig. 9 Contact time impact on the MB dye removal (temperature 30 °C; pH 9; FeNPs — 2.5 mg)



negatively charged MB molecules on the biosorbent surface will repel the remaining MB molecules. This is well supported by the literature [34].

3.9 Methylene blue dye removal using synthesized FeNPs — effect of sorbent dosage

Figure 10 depicts the consequences of the adsorbent dose on the removal of dyes. The efficiency of dye removal improves when the FeNPs dose increases from 0.5 to 2.5 mg. The maximum color removal occurs when the sorbent dosage is 2.5 mg. Even though the color removal is low during the initial period for 1.5 mg dosage, the removal efficiency is found to be increases steadily. As the amount of adsorbent increases, more adsorption sites become available. This results in the percentage hike in color removal. This result is in consistent with literatures [35, 36]. When finding an adsorbent's capability for an adsorbent of specified quantity in a particular working state, the adsorbent dose is a crucial

process component. As adsorbent mass is elevated, dye proportion extracted elevates. This is also well supported by literatures [37, 38].

3.10 Effect of initial dye concentration on MB dye removal using synthesized FeNPs

The rapid interaction among dye concentration and accessible locations on the adsorbent's surface determines the impact of original dye concentration on dye elimination. The quantity of dye that has been adsorbed (mg/g) increases with increase in dye concentration but the proportion of color removal declines. This could be owing to the significant driving power of the initial concentration which is sufficient to overpower the dye mass transfer barrier among phases which are aqueous plus solid [33, 34]. As seen in Fig. 11, the dye initial concentration has a notable impact on sorption. It is also expected that when the dye concentration rises, the dye sorption decreases. Because, the first batch of

Fig. 10 Sorbent's dosage impact on the MB dye removal (time interval — 150 min; temperature 30 °C; pH 9)

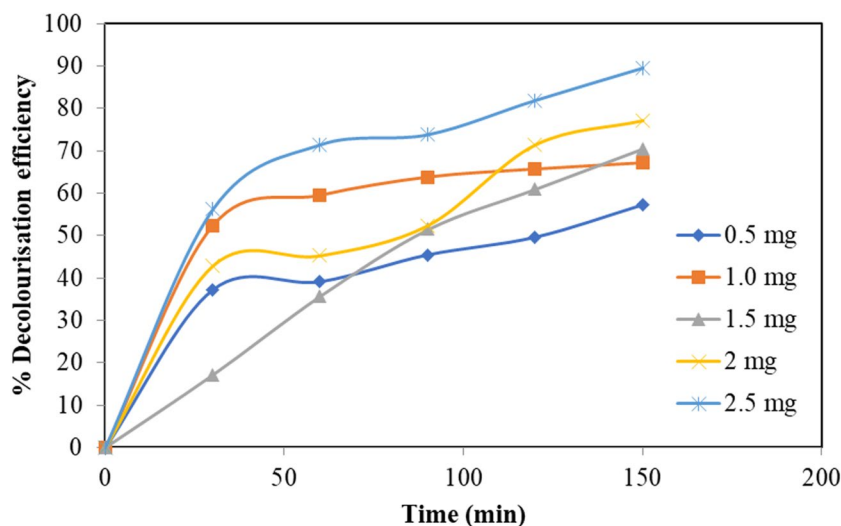
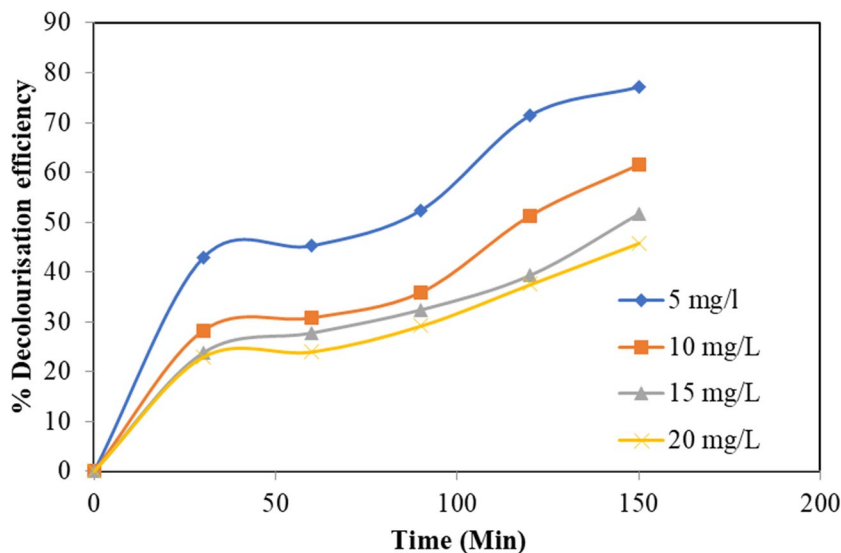


Fig. 11 Initial dye concentration's impact on the MB dye removal (time interval — 150 min; temperature 30 °C; pH 9; FeNPs — 2.5 mg)



pigment molecules fills the pores of surface area, and hence, a decrease in sorption is observed. Hence, dye adsorption is influenced by the initial dye concentration. Similar results were obtained when malachite green was removed with acid-activated low-cost carbon [39–41].

3.11 Equilibrium isotherms

The adsorption isotherm is crucial when designing an adsorption device. Adsorption equilibrium studies aid in the evaluation of adsorbent capacities. The goal of the isotherm research was to understand the relationship between pollutant concentration and adsorbent surfaces, which would aid in improving the utilization of adsorbents for removing pollutants from aqueous solutions. Equilibrium isotherm testing determines the interchange among the adsorbed molecule, and also the sorbent surface. Equilibrium adsorption

isotherms can be seen by plotting a curve between solid phase concentration (mg/g) and liquid phase concentration (mg/L). This study investigated the utility of the Langmuir, Freundlich, Temkin, and Dubinin–Radushkevich (D-R) isotherms in correlating the MB adsorption equilibrium data.

3.11.1 Langmuir isotherm

In 1916, in order to describe gas molecule sorption on metal surfaces, Langmuir [42] suggested a theory, which subsequently extended to include monolayer sorption processes. For single-layer sorption, the Langmuir isotherm relies on the assumption that the adsorbent is uniform and homogeneous and that it adheres to a surface with a large number of open sites [43–47]. The primary flaw in the plan contains that it takes that each site's adsorbent energies are consistent. The following equation represents the Langmuir isotherm.

$$\frac{1}{q_e} = \frac{1}{q_m b C_e} + \frac{1}{q_m} \tag{3}$$

where q_e (mg/g) is the equilibrium quantity adsorbed, C_e (mg/L) is the balance focus, q_m (mg/g) is the maximal potential for multilayer adsorption, b (L/mg) demonstrates the binding site attraction with the Langmuir constant. The RL, which should be less than one for fitness, determines the isotherm’s favorability. It is plotted in Fig. 12a

3.11.2 Freundlich isotherm

Freundlich adsorption isotherms can be applied to diverse surfaces and layered adsorption [44]. It is defined by the variability factor $1/n$. The equation gives the linearized equation for the Freundlich isotherm.

$$\text{Log}q_e = \text{log}K_f + \frac{1}{n}\text{log}C_e \tag{4}$$

where C_e is the equilibrium concentration (mg/L), q_e is the quantity adsorbed at equilibrium (mg/g), and K_f is the Freundlich isotherm strength (mg/g), which varies based on the heterogeneity of the material. $1/n$ is the measure for adsorption strength. The straight line with a intersection of $1/n$ and slope of K_f is produced by plotting $\ln q_e$ vs. $\ln C_e$. n value

defines the sort of either chemical or physical absorption. The plot is given in Fig. 12b

3.11.3 Dubinin–Radushkevich isotherm

Experimental data are utilized in determining whether sorption processes are physical or chemical using the D-R isotherm [48]. As a function of the Polanyi potential, it calculates the adsorbed quantity at equilibrium. The linear form of the D-R isotherm equation is as follows:

$$\ln q_e = \ln q_m - \beta \epsilon^2 \tag{5}$$

where q_e is the quantity of pollutant per weight of adsorbent, adsorbed (mg/g), q_m is the highest potential for sorption (mg/g), β is the coefficient of action linked to mean Swelling energy (mol^2/kJ^2), and Polanyi potential (ϵ) specified as

$$\epsilon = RT \ln \left(1 + \frac{1}{C_e} \right) \tag{6}$$

R is the atomic number (8.314×10^{-3} kJ/mol K), T is the temperature (Kelvin), C_e is the pollutant’s balance in-solution content (mg/L).

The following equation is used to determine the mean free energy of sorption per sorbate molecule required to transport

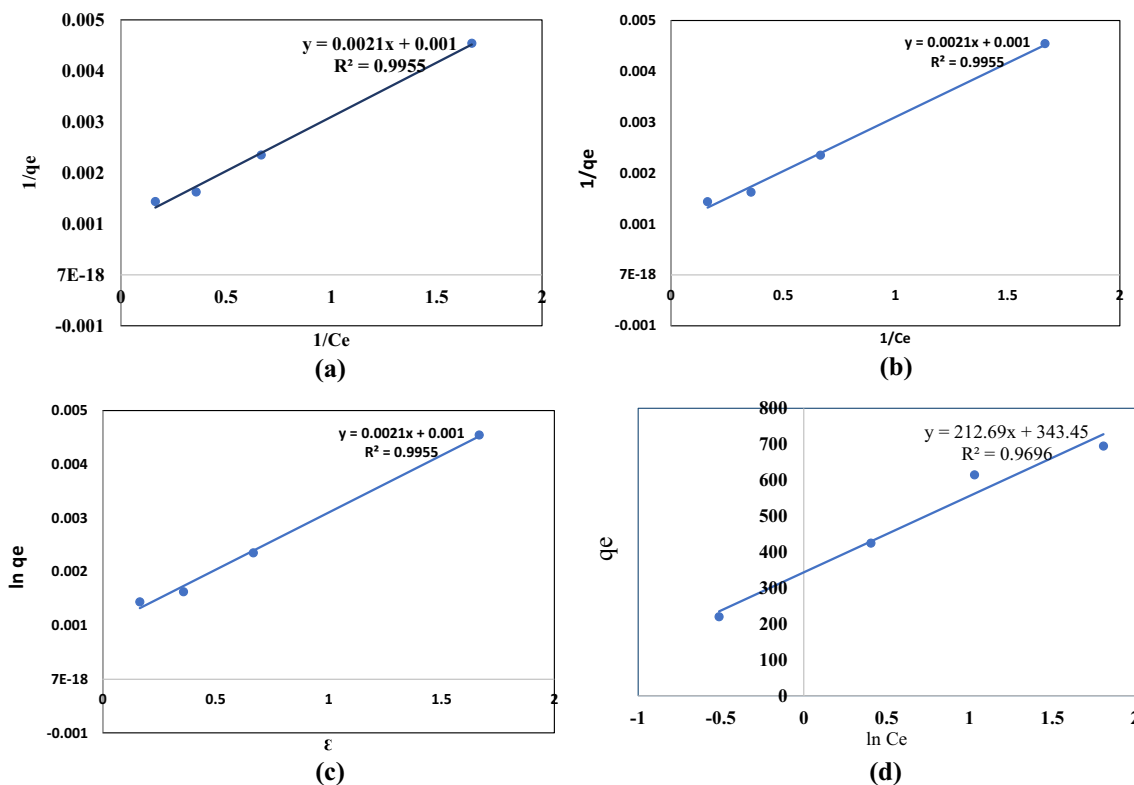


Fig. 12 A Langmuir isotherm, b Freundlich isotherm, c Dubinin–Radushkevich, d Temkin isotherm

one mole of ion from infinite solution to the surface of a nanocomposite:

$$E = \frac{1}{\sqrt{-2\beta}} \tag{7}$$

q_m and the Dubinin–Radushkevich (D-R) isotherm constant calculations are made using the intersection and slope of the $\ln q_e$ plot against \mathcal{E} . For chemical adsorption, the value of E is more than 8 kJ / mol. The energy estimates E value less than 8 kJ/mol indicate that adsorption is a physical process. Figure 12c shows a D-R plot for the MB sorption.

3.11.4 Temkin isotherm

According to the Temkin isotherm equation, adsorption is characterized by a uniform distribution of bonding energies up to the maximal binding energy and that the heat of adsorption of all molecules in a layer declines linearly with coverage due to interactions between the adsorbent and adsorbate [48]. The following equation represents the Temkin isotherm:

$$qe = \frac{RT}{b} \ln(K_T C_e) \tag{8}$$

$$qe = \frac{RT}{b} \ln K_T + \frac{RT}{b} \ln C_e \tag{9}$$

Equation (9) is linearly presented as

$$qe = B \ln K_T + B \ln C_e \tag{10}$$

When plotting $\ln q_e$ against $\ln C_e$, the slope and intercept are used to determine the Temkin isotherm constants.

T the temperature (Kelvin)

R standard gas pressure (kJ/mol K)

K_T binding equilibrium value (L/mg)

b fluctuation of Swelling energy (J/mo)

$B = \frac{RT}{b}$ Temkin constant associated with sorption heat. Figure 12d shows the fit for Temkin isotherm.

3.11.5 Equilibrium studies on the adsorption of MB dye

Studies of isotherm are used better in understanding the link between pollutant concentration and adsorbent surfaces, allowing for more efficient use of adsorbents to filter contaminants out of watery liquids [49, 50]. Isotherm graphs are depicted in Fig. 12. Sorption data from the experiments are suited to all isotherms quite well. The experimental data are well-matched with model prediction when correlation coefficient is more than 0.90. Table 3 depicts pollutant sorption model parameter values, and the R^2 values for linear and nonlinear form. Unlike other R^2 -based isotherms, the Langmuir isotherm suits the MB dye adsorption well. Table 3 contains the isotherm values that were determined from the graph represents the isotherms. The Langmuir isotherm exhibits the greatest coefficient of association of all the isotherms examined ($R^2 > 0.9955$), suggesting that adsorption is a single-layered process. The $1/n$ Freundlich isotherm constant, which varies from 0 to 1, indicates good binding. In this instance, the $1/n$ value of 0.5081 indicates that the sorption was effective. Temkin’s isotherm with a high R^2 number indicates a good match between the model and the data. An E value of 1.63 indicates the sorption is physical. The maximum uptake was found to be 1000 mg/g. Various sorbents used by various researchers and their adsorbent capacity were given in Table 4. From the Table 4, it can be seen that, the synthesized FeNPs has comparable sorption capacity than other sorbents Fig. 13.

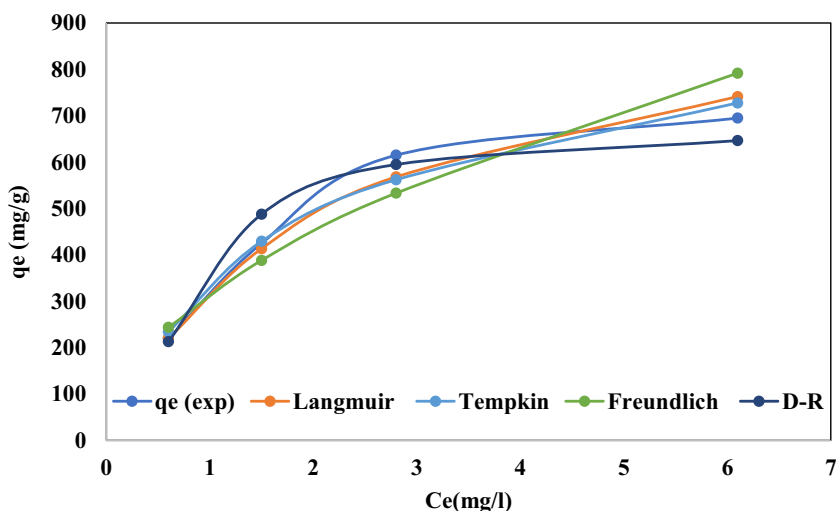
Table 3 Isotherm models factors for methylene blue adsorption

Isotherm	Nonlinear equation	Nonlinear equation parameters	Linear equation parameters
Langmuir isotherm	$q_e = \frac{q_{max} K_L C_e}{1 + K_L C_e}$	q_{max} (mg/g) = 911.7 K_L = 0.470 R^2 = 0.9700	q_{max} (mg/g) = 1000 K_L = 0.6029 R^2 = 0.9955
Freundlich isotherm	$q_e = K_f C_e^{1/n}$	K_f (L/g) = 348.9 $1/n$ = 0.4130 R^2 = 0.9083	K_f (L/g) = 316.01 $1/n$ = 0.5081 R^2 = 0.9148
Dubinin–Radushkevich (D-R) isotherm	$q_e = q_m \exp(-\beta \mathcal{E}^2)$ $\mathcal{E} = RT \ln(1 + 1/C_e)$	q_{max} (mg/g) = 691.5 β (mol ² /kJ ²) = 0.2194 E (kJ/mol) = 1.16 R^2 = 0.9150	q_{max} (mg/g) = 604.25 β (mol ² /kJ ²) = 0.1874 E (kJ/mol) = 1.63 R^2 = 0.9670
Temkin isotherm	$q_e = \frac{RT}{B} \ln(K_T C_e)$	B (J/mol) = 11.85 K_T (L/mg) = 5.027 R^2 = 0.9570	B (J/mol) = 21.69 K_T (L/mg) = 5.0 R^2 = 0.9696

Table 4 Comparison of sorbents material for MB adsorption

S. No	Material	Adsorption capacity (mg/g)	References
1	Indian almond	88.62	[51]
2	Sugarcane bagasse	9.40	[52]
3	MnO ₂ -lignin BC composite	248.96	[53]
5	Wettorrefied microalgal BC	129.57	[54]
5	UiO-66/MIL-101(Fe)-GOCOOH composite	448.70	[55]
6	Banana peel BC/iron oxide composite	862	[56]
7	NaOH/bamboo HC	665.75	[57]
8	FeNPs	1000	This paper

Fig. 13 Isotherm plot for sorption of MB using FeNPs\



3.12 Adsorption kinetics

Kinetic studies explain the speed at which the solute uptake by describing the regulatory driving mechanism. It includes information on reaction pathways and the time it takes to achieve equilibrium. The goal of studying kinetics was to predict total response time, rate-controlling phases, and reaction routes. Kinetics also provides essential details about the adsorbate characteristics both molecular and physical. Several concepts have been proposed to explain the adsorption mechanism. The pseudo-first-order model suggested by Lagergren, the Weber–Morris intraparticle diffusion model, and Ho’s pseudo-second-order model are all used in this research. Both the power function and the Elovich model also used [58–61].

3.12.1 Pseudo first order model

According to the adsorbate and adsorbent, forming a weak connection is exclusively important in physisorption. Linear version of pseudo-first-order kinetics is shown below [62]:

$$\ln(q_e - q_t) = \ln(q_e) - k_1 t \tag{11}$$

where q_e and q_t quantities of pollutant and equilibrium and at time t (mg/g) respectively.

k_1 (1/min) is the pseudo-first-order dynamics rate constant. The parameters of kinetics and correlation coefficient were calculated using the plot t vs. $\log(q_e - q_t)$.

3.12.2 Pseudosecond order model

Pseudo-second order kinetics governs chemisorption [63]. It depicts adsorption process evolution over time.

$$\frac{t}{q_t} = \frac{1}{k_2 q_e^2} + \frac{t}{q_e} \tag{12}$$

q_e and q_t are, both at balance and at time t , the quantities of pollutant ions adsorbed on the adsorbent (mg/g), k_2 is the adsorption rate factor of the second order (g/mg min).

3.12.3 Intraparticle diffusion model

Depending on the intra-particle diffusion model, solute uptake is proportionate to the square bases of contact

time [64]. The below model is used to calculate the kinetic parameters.

$$q_t = k_{id}t^{0.5} + C \quad (13)$$

k_{id} , with C as the coefficient, is the parameter of intraparticle diffusion ($\text{mg}/(\text{g min}^{-0.5})$).

3.12.4 Elovich model

The Elovich model incorporates both the initial adsorption rate ($\text{mg}/\text{g min}$) and the release constant [65]. When comparing Q_t to $\ln(t)$, a connection with an slope of $(1/\beta)$.

$$q_t = \frac{1}{\beta} \ln(\alpha\beta) + \frac{1}{\beta} \ln t \quad (14)$$

where α is the Elovich model constant ($\text{mg g}^{-1} \text{min}^{-1}$), β is the Elovich model exponent (g mg^{-1}).

3.12.5 Power function model

Power functional theory [66] can be expressed as

$$\log q_t = \log k + v \log t \quad (15)$$

The plot of $\log q_t$ against $\log t$ gives the values of v and k .

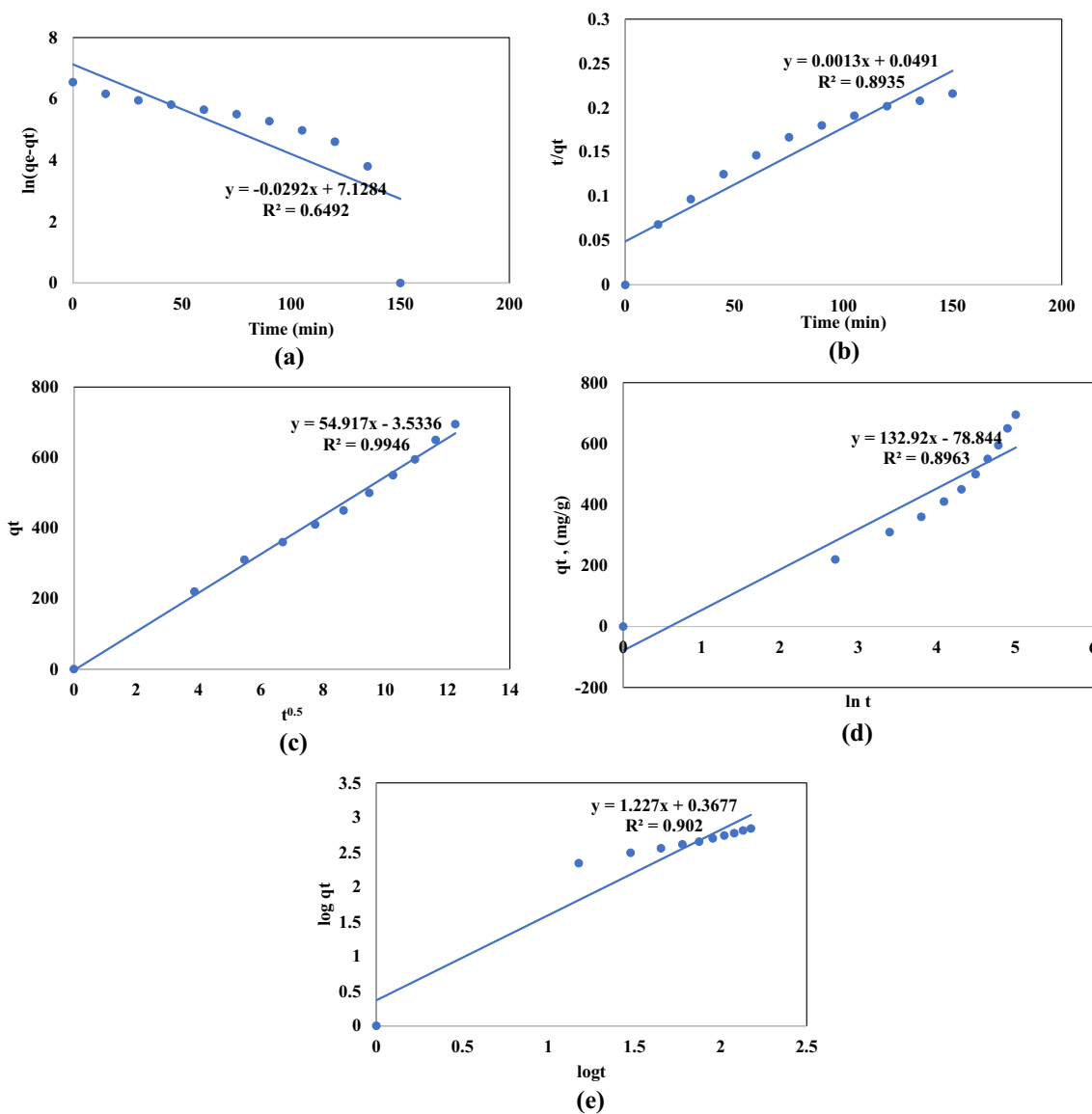
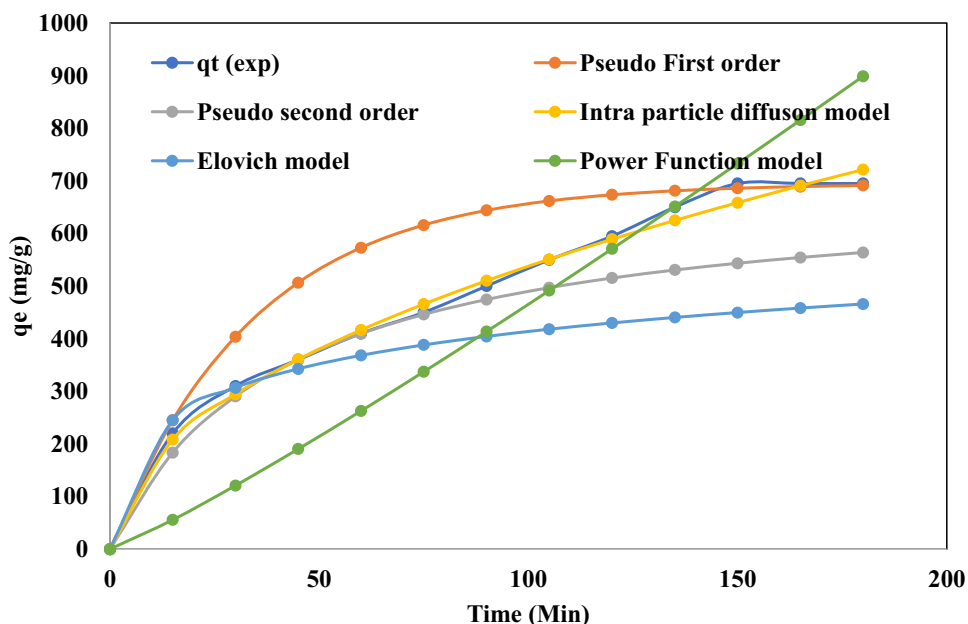


Fig. 14 Adsorption kinetics of MB using iron nano composite **a** pseudofirst order model, **b** pseudosecond order model, **c** diffusion within the particle, **d** model Elovich, and **e** power function models

Fig. 15 Kinetic plot for the sorption of MB using nanocomposite



3.12.6 Kinetics of methylene blue adsorption

Figure 14a–e and Fig. 15 are the linearized kinetics graphs from which the kinetic constants were evaluated. Table 5 lists the rate constants and other parameters. The concept of intra particle diffusions correlation coefficient (R^2) was discovered to be much greater than compared to those of other versions, and the process of adsorption kinetics was controlled by this model.

3.13 Error functions

Five different error functions [67] were utilized in choosing best isotherm models in describing the findings of MB sorption.

3.13.1 Error analysis

Adsorption isotherm parameters was evaluated using error functions in nonlinear regression. They are statistical methods for measuring the discrepancy between model forecasts and experimental evidence [68, 69]. Lowering error value improves predictable models performance. Parameters of adsorption isotherm were estimated by lessening error function by utilizing Microsoft Excel’s solver utility. The five illustrations of error mechanisms are given below:

3.13.2 Some of squares of the errors (ERRSQ/SSE)

The error function that is most usually used is [70]

Table 5 Factors for kinetic simulations of the adsorption of MB using nanocomposite

Kinetics	Nonlinear equation	Nonlinear equation parameters	Linear equation parameters
Pseudofirst order model	$q = q_e(1 - e^{-k_1t})$	$K_1 (\text{min}^{-1}) = 0.0980$ $R^2 = 0.5920$	$K_1 (\text{min}^{-1}) = 0.0298$ $R^2 = 0.6492$
Pseudo second order model	$q = \frac{q_e^2 k_2 t}{1 + q_e k_2 t}$	$K_2 ((\text{g}/\text{mg}) \text{ min}) = 0.00002443$ $R^2 = 0.9836$	$K_2 ((\text{g}/\text{mg}) \text{ min}) = 0.0000344$ $R^2 = 0.8935$
Intraparticle diffusion model	$q_e = k_{id} t^{0.5}$	$K_{id} ((\text{mg}/\text{g}) \text{ min}^{-0.5}) = 53.58$ $R^2 = 0.9971$	$K_{id} ((\text{mg}/\text{g}) \text{ min}^{-0.5}) = 26.414$ $R^2 = 0.9946$
Elovich model	$q_t = \frac{1}{\beta} \ln(1 + \alpha\beta t)$	$\beta (\text{g}/\text{mg}) = 0.0023$ $\alpha (\text{mg}/\text{g} \text{ min}) = 25.27$ $R^2 = 0.9886$	$\beta (\text{g}/\text{mg}) = 0.00991$ $\alpha (\text{mg}/\text{g} \text{ min}) = 69.743$ $R^2 = 0.8963$
Power function model	$qt = kt^v$	$K = 3.0$ $V = 1.136$ $R^2 = 0.9670$	$K = 2.67$ $V = 1.1691$ $R^2 = 0.9020$

$$\sum_{i=1}^n (q_{e,cal} - q_{e,exp})_i^2 \quad (16)$$

3.13.3 Hybrid fractional error function (HYBRID) [71]

For improving fit at less concentrations, it is typical to divide the squares sum of errors by the value which had been calculated. The isotherm equation also employs the amount of systems degrees of freedom as a divisor which is the sum of the factors and the number of data elements n and p .

$$\frac{100}{n-p} \sum_{i=1}^n \left[\frac{q_{e,exp} - q_{e,cal}}{q_{e,exp}} \right]_i \quad (17)$$

3.13.4 Marquardt's percent standard deviation [72]

An error distribution with a cubic mean is resembled by Marquardt's percent standard deviation (MPSD) in certain aspects, but it is modified for the total amount of possible device configurations.

$$100 \sqrt{\frac{1}{n-p} \sum_{i=1}^n \left[\frac{q_{e,exp} - q_{e,cal}}{q_{e,exp}} \right]_i^2} \quad (18)$$

3.13.5 Average relative error

The error function works to keep the fractional error distribution constant as minimal as feasible throughout the concentration range [73, 74]

$$\frac{100}{n} \sum_{i=1}^n \left| \frac{q_{e,exp} - q_{e,cal}}{q_{e,exp}} \right|_i \quad (19)$$

3.13.6 Sum of absolute errors (EABS/SAE)

As the amount of the error increases, the factors produced by using this error function produce a superior fit, tipping the fit in favor of data with greater concentrations. Tables 6 and 7 contain the values for adsorption isotherm factors and single-system error analysis.

Table 6 Adsorption isotherm factors and single-system error analysis

	ERRSQ/ SSE	HYBRID	MPSD	ARE	EABS/ SAE
Langmuir	4473.86	1.22	6.05	3.40	104.72
Freundlich	18,009.94	-0.94	13.70	9.34	239.25
D-R	6770.63	-0.45	9.81	5.65	138.62
Temkin	6738.09	-1.37	8.60	5.58	143.52

Table 7 Adsorption isotherm factors and single-system nonlinear error analysis

	ERRSQ/ SSE	HYBRID	MPSD	ARE	EABS/ SAE
Langmuir	12,452.8	12.88	18.48	1.769	183.40
Freundlich	12,360.78	-6.06	18.48	10.09	197.48
D-R	5317.07	2.89	4.88	7.03	127.15
Temkin	4063.86	-1.33	6.86	4.2	104.46

$$\sum_{i=1}^n |q_{e,exp} - q_{e,cal}|_i \quad (20)$$

where, $q_{e,calc}$ is the estimated equilibrium adsorbate content, (mg/g); $q_{e,exp}$ is the maximum adsorbate quantity as determined by experiment, (mg/g).

The results of the error function values were compared and concluded that HYBRID model generated greater results of the error functions investigated. According to the HYBRID error model, Temkin offered a better match than other models.

4 Conclusions

A conventional and practical method of fabrication of iron nanoparticles using a novel green pathway employing jujube leaf extract was established in this work. The authenticity of nanoparticle synthesis was confirmed through SEM, TEM, and XRD results. The FeNPs that were produced were in the range of 10 to 30 nm in size with an average size of 20 nm. The decolorization of methylene blue is performed using the FeNPs, and a maximum of about 89.5% was attained. The Langmuir model was found to be the most accurate, with a maximum adsorption capacity of q_{max} (1000 mg/g). The results of adsorption kinetics showed that adsorption followed pseudo second-order kinetic equation for sorption of methylene blue onto synthesized nanoparticles. This research work provide a new technique for the controlled combination of size and shape-dependent iron nanoparticles, which can be used to treat dye effluent from textiles and other chemical industries. The technique employed in this study for the synthesis of FeNPs was simple, quick, low-cost, and environmentally benign, as it did not use any organic solvents or other harmful chemicals. In conclusion, this study has demonstrated the effectiveness of using adsorbing reagents (biosorbents) made from inexpensive, readily available, biodegradable, and non-hazardous materials to remove dyes like MB before they are dumped into the environment.

Acknowledgements The authors are thankful to the Bharathidasan Institute of Technology (BIT) Campus, Anna University,

Trichirapalli-620 024 and Annamalai University, Annamalai nagar, Chidambaram, India, for the technical support.

Author contribution All authors contributed to the study conception and design. All authors edited and approved the final version of the manuscript.

Data availability The dataset generated and/or analyzed during the current study are available from the corresponding author [M. Rengasamy], upon reasonable request.

Declarations

Ethical approval and consent to participate Not applicable.

Consent of publication Not applicable.

Competing interest The authors declare no competing interests.

References

- Oraon A, Prajapati AK, Ram M, Saxena VK, Dutta S (2022) Gupta AK (2022) Synthesis, characterization, and application of microporous biochar prepared from *Pterospermum acerifolium* plant fruit shell waste for methylene blue dye adsorption: the role of surface modification by SDS surfactant. *Biomass Conv Bioref.* <https://doi.org/10.1007/s13399-022-02320-8>
- Afsheen S, Tahir MB, Iqbal T, Liaqat A, Abrar M (2018) Green synthesis and characterization of novel iron particles by using different extracts. *J Alloys Compd* 732:935–944
- Supee AH, Zaini MAA (2022) Phosphoric acid-activated bamboo hydrochar for methylene blue adsorption: isotherm and kinetic studies. *Biomass Conv Bioref.* <https://doi.org/10.1007/s13399-022-03465-2>
- El-Shamy AG (2020) An efficient removal of methylene blue dye by adsorption onto carbon dot @ zinc peroxide embedded poly vinyl alcohol (PVA/CZnO₂) nano-composite: a novel reusable adsorbent. *Polymer (Guildf)* 202:122565. [10.1016/j.polymer.2020.122565](https://doi.org/10.1016/j.polymer.2020.122565)
- Bharathi D, Nandagopal JGT, Ranjithkumar R, Gupta PK, Djearamane S (2022) Microbial approaches for sustainable remediation of dye-contaminated wastewater: a review. *Arch Microbiol* 204(3):1–11. <https://doi.org/10.1007/s00203-022-02767-3>
- Arularasu MV, Anbarasu M, Poovaragan S, Sundaram R, Kanimozhi K, Magdalane CM, Kaviyarasu K, Thema FT, Letsholathebe D, Mola GT, Maaza M (2018) Structural, optical, morphological and microbial studies on SnO₂ nanoparticles prepared by co-precipitation method. *J Nanosci Nanotechnol* 18:3511–3517. <https://doi.org/10.1166/jnn.2018.1465>
- Holliday MC, Parsons DR (2022) Zein SH (2022) Agricultural pea waste as a low-cost pollutant biosorbent for methylene blue removal: adsorption kinetics, isotherm and thermodynamic studies. *Biomass Conv Bioref.* <https://doi.org/10.1007/s13399-022-02865-8>
- Saha N, Das L, Das P, Bhowal A, Bhattacharjee C (2021) Comparative experimental and mathematical analysis on removal of dye using raw rice husk, rice husk charcoal and activated rice husk charcoal: batch, fixed-bed column, and mathematical modeling. *Biomass Convers Biorefinery.* <https://doi.org/10.1007/s13399-021-01996-8>
- Tharani K, Jegatha Christy A, Sagadevan S, Nehru LC (2021) Photocatalytic and antibacterial performance of iron oxide nanoparticles formed by the combustion method. *Chem Phys Lett* 771:138524. <https://doi.org/10.1016/j.cplett.2021.138524>
- Paluri P, Ahmad KA, Durbha KS (2022) Importance of estimation of optimum isotherm model parameters for adsorption of methylene blue onto biomass derived activated carbons: comparison between linear and non-linear methods. *Biomass Conv Bioref* 12:4031–4048. <https://doi.org/10.1007/s13399-020-00867-y>
- Goswami M, Baruah D, Das AM (2018) Green synthesis of silver nanoparticles supported on cellulose and their catalytic application in the scavenging of organic dyes. *New J Chem* 42(13):10868–10878
- Raj S, Chand Mali S, Trivedi R (2018) Green synthesis and characterization of silver nanoparticles using *Enicostemma axillare* (Lam.) leaf extract. *Biochem Biophys Res Commun* 503:2814–2819. <https://doi.org/10.1016/j.bbrc.2018.08.045>
- Razali NS, Abdulhameed AS, Jawad AH, ALOthman ZA, Yousef TA, Al-Duaij OK, Alsaiari NS, (2022) High-surface-area-activated carbon derived from mango peels and seeds wastes via microwave-induced ZnCl₂ activation for adsorption of methylene blue dye molecules: statistical optimization and mechanism. *Molecules* 27:6947. <https://doi.org/10.3390/molecules27206947>
- Suppiah DD, MuhdJulkapli N, Sagadevan S, Johan MR (2023) Eco-friendly green synthesis approach and evaluation of environmental and biological applications of iron oxide nanoparticles. *Inorg Chem Commun* 152:110700. <https://doi.org/10.1016/j.inoche.2023.110700>
- Selvam K, Sudhakar C, Govarthanam M, Thiyagarajan P, Sengottaiyan A, Balakrishnan S (2017) Eco-friendly biosynthesis and characterization of silver nanoparticles using *Tinosporacordifolia* (Thunb.) Miers and evaluate its antibacterial, antioxidant potential. *J Radiat Res Appl Sci* 10:6–12. <https://doi.org/10.1016/j.jrras.2016.02.005>
- Belcaid A, Beakou BH, Bouhsina S, Anouar A (2022) Insight into adsorptive removal of methylene blue, malachite green, and rhodamine B dyes by cassava peel biochar (*Manihot esculenta* Crantz) in single, binary, and ternary systems: competitive adsorption study and theoretical calculations. *Biomass Conv Bioref.* <https://doi.org/10.1007/s13399-022-02928-w>
- Abdulhameed AS, Jawad AH, Kashi E, Radzun KA, Zeid A, ALOthman, Lee D, Wilson, (2022) Insight into adsorption mechanism, modeling, and desirability function of crystal violet and methylene blue dyes by microalgae: Box-Behnken design application. *Algal Res* 67:102864. <https://doi.org/10.1016/j.algal.2022.102864>
- Fadillah G, Yudha SP, Sagadevan S, Fatimah Is, Muraza O (2020) Magnetic iron oxide/clay nanocomposites for adsorption and catalytic oxidation in water treatment applications. *Open Chemistry*. 18(1):1148–1166. <https://doi.org/10.1515/chem-2020-0159>
- Fatimah Is, Purwiandono G, Hidayat A, Sagadevan S, Kamari A (2022) Mechanistic insight into the adsorption and photocatalytic activity of a magnetically separable γ -Fe₂O₃/Montmorillonite nanocomposite for rhodamine B removal. *Chem Phys Lett* 792:139410. <https://doi.org/10.1016/j.cplett.2022.139410>
- Tobaldi DM, Seabra MP, Novais RM, Ascens G (2018) Biomass fly ash geopolymer monoliths for effective methylene blue removal from wastewaters. *J Clean Prod* 171:783–794
- Foo KY, Hameed BH (2010) Insights into the modeling of adsorption isotherm systems. *Rev Chem Eng* 156:2–10
- Golmohammadi M, Honarmand M, Esmaili A (2022) Biosynthesis of ZnO nanoparticles supported on bentonite and the evaluation of its photocatalytic activity. *Mater Res Bull* 149:111714. <https://doi.org/10.1016/j.materresbull.2021.111714>
- Alharthi MN, Ismail I, Bellucci S, Jaremko M, Salah EM, Abo-Aba MA, Salam, (2023) Biosynthesized zinc oxide nanoparticles using *Ziziphus jujube* plant extract assisted by ultrasonic

- irradiation and their biological applications. *Separations* 10(2):78. <https://doi.org/10.3390/separations10020078>
24. Alharthi MN, Ismail I, Bellucci S, Salam MA (2021) Green synthesis of zinc oxide nanoparticles by *Ziziphus jujuba* leaves extract: environmental application, kinetic and thermodynamic studies. *J Phys Chem Solids* 158:110237. <https://doi.org/10.1016/j.jpcs.2021.110237>
 25. Aisida SO, Madubuonu N, Alnasir MH, Ahmad I, Botha S, Mazza M, Ezema FI (2020) Biogenic synthesis of iron oxide nanorods using *Moringa oleifera* leaf extract for antibacterial applications. *Appl Nanosci* 10:305–315. <https://doi.org/10.1007/s13204-019-01099-x>
 26. Hanafi NAM, Abdulhameed AS (2022) Jawad AH (2022) Optimized removal process and tailored adsorption mechanism of crystal violet and methylene blue dyes by activated carbon derived from mixed orange peel and watermelon rind using microwave-induced $ZnCl_2$ activation. *Biomass Conv Bioref*. <https://doi.org/10.1007/s13399-022-03646-z>
 27. Sagadevan S, Sivasankaran RP, Lett JA, Fatimah I, Weldegebrical GK, Léonard E, Le M-V, Soga T (2023) Evaluation of photocatalytic activity and electrochemical properties of hematite nanoparticles. *Symmetry* 15:1139. <https://doi.org/10.3390/sym15061139>
 28. Uddin MK, Malek NNA, Jawad AH, Sabar S (2023) Pyrolysis of rubber seed pericarp biomass treated with sulfuric acid for the adsorption of crystal violet and methylene green dyes: an optimized process. *Int J Phytoremediation* 25(4):393–402. <https://doi.org/10.1080/15226514.2022.2086214>
 29. Wang B, Jia M, Fang L, Jiang L, Li Y (2018) Effects of eucalyptus oil and anise oil supplementation on rumen fermentation characteristics, methane emission, and digestibility in sheep. *J Anim Sci* 96(8):3460–3470. <https://doi.org/10.1093/jas/sky216>
 30. De Araujo TP, Tavares FO, Vareschini DT, Barros M (2020) Biosorption mechanisms of cationic and anionic dyes in a low-cost residue from brewer's spent grain. *Environ Technol*. 42(19):1–16. <https://doi.org/10.1080/09593330.2020.1718217>
 31. Bo L, Gao F, Shuangbao BY, Liu Z, Dai Y (2021) A novel adsorbent *Auricularia Auricular* for the removal of methylene blue from aqueous solution: isotherm and kinetics studies. *Environ Technol&Innov* 23:101576. <https://doi.org/10.1016/j.eti.2021.101576>
 32. Georgin J, Franco DSP, Netto MS, Allasia D, Oliveira MLS, Dotto GL (2020) Treatment of water containing methylene by biosorption using Brazilian berry seeds (*Eugenia uniflora*). *Environ Sci Pollut Res*. 27(17):20831–20843. <https://doi.org/10.1007/s11356-020-08496-8>
 33. Cusioli LF, Quesada HB, Baptista ATA, Gomes RG, Bergamasco R (2020) Soybean hulls as a low-cost biosorbent for removal of methylene blue contaminant. *Environ Prog Sustain Energy* 39(2):13328. <https://doi.org/10.1002/ep.13328>
 34. Al-Mahmoud S (2020) Kinetic and thermodynamic studies for the efficient removal of methylene blue using *Hordeum Murinum* as a new biosorbent. *Egypt J Chem* 63(9):3381–3390. <https://doi.org/10.21608/ejchem.2020.16008.1970>
 35. Sulyman M, Namiesnik J, Gierak A (2017) Low-cost adsorbents derived from agricultural by-products/wastes for enhancing contaminant uptakes from wastewater: a review. *Pol J Environ Stud* 26(2):479–510
 36. Tempkin MI, Pyzhev V (1940) Kinetics of ammonia synthesis on promoted iron catalyst. *Acta Phys Chim USSR* 12:327–356
 37. Machado S, Pacheco JG, Nouws HP, Albergaria JT, Delerue-Matos C (2015) Characterization of green zero-valent iron nanoparticles produced with tree leaf extracts. *Sci Total Environ* 533:76e81
 38. Machado S, Pacheco JG, Nouws HPA, Albergaria JT, Delerue-Matos C (2015) Characterization of green zero-valent iron nanoparticles produced with tree leaf extracts. *Sci Total Environ* 533:76–81. <https://doi.org/10.1016/j.scitotenv.2015.06.091>
 39. Mahmoud AA, El-Feky GS, Kamel R, Awad GEA (2011) Chitosan/ sulfobutylether- β -cyclodextrin nanoparticles as a potential approach for ocular drug delivery. *Int J Pharm* 413:229–236. <https://doi.org/10.1016/j.ijpharm.2011.04.031>
 40. Mohan Kumar K, Mandal BK, Siva Kumar K, Sreedhara Reddy P, Sreedhar B (2013) Biobased green method to synthesise palladium and iron nanoparticles using Terminalia chebula aqueous extract. *Spectrochim Acta - Part A Mol Biomol Spectrosc* 102:128–133. <https://doi.org/10.1016/j.saa.2012.10.015>
 41. Nassar MY, Abdelrahman EA (2017) Hydrothermal tuning of the morphology and crystallite size of zeolite nanostructures for simultaneous adsorption and photocatalytic degradation of methylene blue dye. *J Mol Liq* 242:364–374
 42. Langmuir I (1916) The constitution and fundamental properties of solids and liquids. *J Am Chem Soc* 38(11):2221
 43. Hashem AH, Saied E, Hasanin MS (2020) Green and eco-friendly bio-removal of methylene blue dye from aqueous solution using biologically activated banana peel waste. *Sustain Chem Pharm* 18:100333. <https://doi.org/10.1016/j.scp.2020.100333>
 44. Mythili R, Selvankumar T, Kamala-Kannan S, Sudhakar C, Ameen F, Al-Sabri A, Selvam K, Govarthanan M, Kim H (2018) Utilization of market vegetable waste for silver nanoparticle synthesis and its antibacterial activity. *Mater Lett* 225:101–104. <https://doi.org/10.1016/j.matlet.2018.04.111>
 45. Aljeboree AM, Al-Baitai AY, Abdalhadi SM, Alkaim AF (2021) Investigation study of removing methyl violet dye from aqueous solutions using corn-cob as a source of activated carbon. *Egypt J Chem* 64(6):2873–2878. <https://doi.org/10.21608/ejchem.2021.55274.3159>
 46. Praveen A, Lakshmi Narayana Rao G, Balakrishna B (2018) Performance and emission characteristics of a diesel engine using *Calophyllum Inophyllum* biodiesel blends with TiO_2 nanoadditives and EGR. *Egypt J Pet* 27(4):731–738. <https://doi.org/10.1016/j.ejpe.2017.10.008>
 47. Maleki A, Mohammad M, Emdadi Z, Asim N, Azizi M, Safaei J (2018) Adsorbent materials based on a geopolymer paste for dye removal from aqueous solutions. *Arab J Chem* 13(1):3017–3025
 48. Abdelrahman EA (2018) Synthesis of zeolite nanostructures from waste aluminum cans for efficient removal of malachite green dye from aqueous media. *J Mol Liq* 253:72–82
 49. Dastoorian F, Salem A, Salem S (2018) Fabrication of poorly crystalline hydroxyapatite nano-particles by rapid auto-ignition route as efficient adsorbent for removal of disperse blue dye. *J Alloys Compd* 766:729–738
 50. Freundlich HMF (1906) Over the adsorption in solution. *J Phys Chem* 57:385–471
 51. Hevira L, Zilfa R, Ighalo JO, Aziz H, Zein R (2021) Terminalia catappa shell as low-cost biosorbent for the removal of methylene blue from aqueous solutions. *J Ind Eng Chem* 97:188–199. <https://doi.org/10.1016/j.jiec.2021.01.028>
 52. Siqueira TCA, de Silva IZ, Rubio AJ, Bergamasco R, Gasparotto F, Paccola EAS, Yamaguchi NU (2020) Sugarcane bagasse as an efficient biosorbent for methylene blue removal: kinetics, isotherms and thermodynamics. *Int J Environ Res Public Health* 17:526. <https://doi.org/10.3390/ijerph17020526>
 53. Liu X-J, Li M-F, Singh SK (2021) Manganese-modified lignin biochar as adsorbent for removal of methylene blue. *J Market Res* 12:1434–1445
 54. Yu KL, Lee XJ, Ong HC, Chen W-H, Chang J-S, Lin C-S, Show PL, Ling TC (2021) Adsorptive removal of cationic methylene blue and anionic Congo red dyes using wet-torrefied microalgal biochar: Equilibrium, kinetic and mechanism modeling. *Environ Pollut* 272:115986

55. Zhang P, O'Connor D, Wang Y, Jiang L, Xia T, Wang L, Tsang DC, Ok YS, Hou D (2020) A green biochar/iron oxide composite for methylene blue removal. *J Hazard Mater* 384:121286
56. Qian W-C, Luo X-P, Wang X, Guo M, Li B (2018) Removal of methylene blue from aqueous solution by modified bamboo hydrochar. *Ecotoxicol Environ Saf* 157:300–306
57. Eltaweil AS, Abd El-Monaem EM, El-Subruiti GM, Abd El-Latif MM, Omer AM (2020) Fabrication of UiO-66/MIL-101 (Fe) binary MOF/carboxylated-GO composite for adsorptive removal of methylene blue dye from aqueous solutions. *RSC Adv* 10(32):19008–19019
58. Dubinin MM (1960) The potential theory of adsorption of gases and vapors for adsorbents with energetically nonuniform surfaces. *Chem Rev* 60(2):235–241
59. Agarwal S, Tyagi I, Gupta VK, Ghasemi N, Shahivand M, Ghasemi M (2016) Kinetics, equilibrium studies and thermodynamics of methylene blue adsorption on Ephedra strobilacea saw dust and modified using phosphoric acid and zinc chloride. *J Mol Liq* 218:208–218
60. Li B, Gan L, Owens G, Chen Z (2018) New nano-biomaterials for the removal of malachite green from aqueous solution via a response surface methodology. *Water Res* 146:55–66
61. Sharma A, Siddiqui ZM, Dhar S, Mehta P (2019) Adsorptive removal of congo red dye (CR) from aqueous solution by *Cornulacamonacantha* stem and biomass-based activated carbon: isotherm, kinetics and thermodynamics. *Sep Sci Technol* 54:916–929
62. Ho YS, McKay G (1999) Pseudo-second order model for sorption processes. *Process Biochem* 34:451–465
63. Ho YS (2004) Citation review of Lagergren kinetic rate equation on adsorption reactions. *Scientometrics* 59:171–177. <https://doi.org/10.1023/B:SCIE.0000013305.99473.cf>
64. Sengottaiyan A, Aravinthan A, Sudhakar C, Selvam K, Srinivasan P, Govarthanan M, Manoharan K, Selvakumar T (2016) Synthesis and characterization of *Solanum nigrum*-mediated silver nanoparticles and its protective effect on alloxan-induced diabetic rats. *J Nanostructure Chem* 6:41–48. <https://doi.org/10.1007/s40097-015-0178-6>
65. Gupta T, Lataye D (2019) Removal of crystal violet and methylene blue dyes using *Acacia nilotica* sawdust activated carbon. *Indian J Chem Technol* 26:52–68
66. Mane VS, Mall ID, Srivastava VC (2007) Kinetic and equilibrium isotherm studies for the adsorptive removal of Brilliant Green dye from aqueous solution by rice husk ash. *J Environ Manage* 84:390–400
67. Wang T, Jin X, Chen Z et al (2014) Green synthesis of Fe nanoparticles using eucalyptus leaf extracts for treatment of eutrophic wastewater. *Sci Total Environ* 466–467:210–213. <https://doi.org/10.1016/j.scitotenv.2013.07.022>
68. Wang T, Lin J, Chen Z, Megharaj M, Naidu R (2014) Green synthesized iron nanoparticles by green tea and eucalyptus leaves extracts used for removal of nitrate in aqueous solution. *J Clean Prod* 83:413e419
69. Wang W-L, Cai Y-Z, Hu H-Y, Chen J, Wang J, Xue G, Wu Q-Y (2019) Advanced treatment of bio-treated dyeing and finishing wastewater using ozonebiological activated carbon: a study on the synergistic effects. *Chem. Eng J* 359:168e175
70. Weber WJ, Morris JC (1963) Kinetics of adsorption on carbon from solutions. *J Sanit Eng Div* 89:31–39
71. Weng X, Huang L, Chen Z, Megharaj M, Naidu R (2013) Synthesis of iron-based nanoparticles by green tea extract and their degradation of malachite. *Ind Crop Prod* 51:342e347
72. Xiao Z, Zhang H, Xu Y, Yuan M, Jing X, Huang J, Li Q, Sun D (2017) Ultraefficient removal of chromium from aqueous medium by biogenic iron based nanoparticles. *Separ Purif Technol* 174:466e473
73. Martinez CLM, Sermyagina E, JussiSaari MS, de Jesus M, Cardoso GM, de Almeida EsaVakkilainen (2021) Hydrothermal carbonization of lignocellulosic agro-forest based biomass residues. *Biomass Bioenergy* 147:106004. <https://doi.org/10.1016/j.biombioe.2021.106004>
74. Zhang L, Sellaoui L, Franco D, Dotto GL, Bajahzar A, Belmabrouk H, Bonilla Petriciolet A, Oliveira MLS, Li Z (2020) Adsorption of dyes brilliant blue, sunset yellow and tartrazine from aqueous solution on chitosan: analytical interpretation via multilayer statistical physics model. *Chem Eng J* 382:122952

Publisher's Note Springer Nature remains neutral with regard to jurisdictional claims in published maps and institutional affiliations.

Springer Nature or its licensor (e.g. a society or other partner) holds exclusive rights to this article under a publishing agreement with the author(s) or other rightsholder(s); author self-archiving of the accepted manuscript version of this article is solely governed by the terms of such publishing agreement and applicable law.